AFRL-RV-PS-
TR-2017-0068

AFRL-RV-PS-
TR-2017-0068

CHARACTERIZATION OF CARRIER TRANSPORT PROPERTIES IN STRAINED CRYSTALLINE Si WALL-LIKE STRUCTURES AS A FUNCTION OF SCALING INTO THE QUASI-QUANTUM REGIME

Naz Islam

University of Missouri
Electrical and Computer Engineering
319 Engineering Building West
Columbia, MO 65211

3 May 2017

Final Report

APPROVED FOR PUBLIC RELEASE; DISTRIBUTION IS UNLIMITED.

AIR FORCE RESEARCH LABORATORY
Space Vehicles Directorate
3550 Aberdeen Ave SE
AIR FORCE MATERIEL COMMAND
KIRTLAND AIR FORCE BASE, NM 87117-5776

REPORT DOCUMENTATION PAGE

Form Approved
OMB No. 0704-0188

Public reporting burden for this collection of information is estimated to average 1 hour per response, including the time for reviewing instructions, searching existing data sources, gathering and maintaining the data needed, and completing and reviewing this collection of information. Send comments regarding this burden estimate or any other aspect of this collection of information, including suggestions for reducing this burden to Department of Defense, Washington Headquarters Services, Directorate for Information Operations and Reports (0704-0188), 1215 Jefferson Davis Highway, Suite 1204, Arlington, VA 22202-4302. Respondents should be aware that notwithstanding any other provision of law, no person shall be subject to any penalty for failing to comply with a collection of information if it does not display a currently valid OMB control number. **PLEASE DO NOT RETURN YOUR FORM TO THE ABOVE ADDRESS.**

1. REPORT DATE *(DD-MM-YYYY)*	2. REPORT TYPE	3. DATES COVERED *(From - To)*
03-05-2017	Final Report	2 Dec 2009 – 1 May 2017

4. TITLE AND SUBTITLE

Characterization of Carrier Transport Properties in Strained Crystalline Si Wall-Like Structures as a Function of Scaling into the Quasi-Quantum Regime

5a. CONTRACT NUMBER FA9453-10-1-0001

5b. GRANT NUMBER

5c. PROGRAM ELEMENT NUMBER 62601F

5d. PROJECT NUMBER 4846

5e. TASK NUMBER PPM00010287

5f. WORK UNIT NUMBER EF001022

6. AUTHOR(S)

Naz Islam

7. PERFORMING ORGANIZATION NAME(S) AND ADDRESS(ES)

University of Missouri
Department of Electrical and Computer Engineering
319 Engineering Building West
Columbia, MO 65211

8. PERFORMING ORGANIZATION REPORT NUMBER

9. SPONSORING / MONITORING AGENCY NAME(S) AND ADDRESS(ES)

Air Force Research Laboratory
Space Vehicles Directorate
3550 Aberdeen Ave., SE
Kirtland AFB, NM 87117-5776

10. SPONSOR/MONITOR'S ACRONYM(S) AFRL/RVSW

11. SPONSOR/MONITOR'S REPORT NUMBER(S) AFRL-RV-PS-TR-2017-0068

12. DISTRIBUTION / AVAILABILITY STATEMENT

Approved for public release; distribution is unlimited.

13. SUPPLEMENTARY NOTES

14. ABSTRACT

This research focused on transport characteristics of electrons and holes through narrow constricted crystalline Si "wall-like" long-channels that were surrounded by a thermally grown SiO_2 layer. The strained buffering depth inside the Si region (due to Si/SiO_2 interfacial lattice mismatch) is where scattering is seen to enhance some modes of the carrier-lattice interaction, while suppressing others, thereby changing the relative value of the carrier's effective masses of both electrons and holes, as compared to bulk Si. Importantly, as a result of the existence of fixed oxide charges in the thermally grown SiO_2 layer and the Si/SiO_2 interface, the effective Si cross-sectional wall widths were considerably narrower than the actual physical widths, due to the formation of depletion regions from both sides. The physical height of the crystalline-Si structures was 1500 nm, and the widths were incrementally scaled down from 200 nm to 20 nm. These nanostructures were configured into a metal-semiconductor-metal device configuration that was isolated from the substrate region. In the narrowest wall devices, a considerable increase in conductivity was observed as a result of higher carrier mobilities due to lateral constriction and strain.

15. SUBJECT TERMS

Semiconductor Nanostructures,Quantum Confinement, Ballistic Transport, Interfacial Strain Effects, Carrier Mobility

16. SECURITY CLASSIFICATION OF:			17. LIMITATION OF ABSTRACT	18. NUMBER OF PAGES	19a. NAME OF RESPONSIBLE PERSON
					Ashwani Sharma
a. REPORT	b. ABSTRACT	c. THIS PAGE	Unlimited	34	19b. TELEPHONE NUMBER *(include area code)*
Unclassified	Unclassified	Unclassified			

pre-device mesa structure. After the walls were oxidized to achieve the desired wall width, the thermally grown oxide was selectively removed from the planar un-textured Si pad locations [Figure 3(b)] using an appropriate photo-mask and a chemical 1:6 buffered oxide etch (BOE) process.

Following the resist removal the samples were cleaned using a sulfuric-acid:hydrogen-peroxide solution and a DI water rinse followed by a nitrogen gas dry step. The samples were then re-patterned using photoresist and a second mask was used for the process to form the electrode contact regions. Three separate evaporations (30 nm of Ni) were performed. The first one was performed at a normal incidence to the sample surface and the other two at a 30o degree tilt angles in order to ensure complete coverage of the mesa step height. After Ni evaporation, lift-off was performed to remove the unwanted metal and resist using acetone. Following a thorough clean using methanol/DI-water, the samples were again dehydrated and spin-coated with a thick resist layer. The samples were patterned using a final metallization mask set. A layer of Cr and Au was evaporated on the electrode regions. 30 nm/200 nm of Cr/Au were evaporated and liftoff process was used to remove the resist and unwanted metal. Figure 3(c) shows SEM pictures of a fully fabricated wall device.

3.4 DC measurements

At room temperature only a small number of carriers are thermally generated (as dark current) for a Si bandgap of 1.15 eV. At low bias voltages (linear region of operation) the slope of the I-V dark current is proportional to the device resistance that includes contributions of thermally generated carriers from both the wall channels and the metal/semiconductor contact regions. At higher biases the current saturates when all thermally generated carriers are collected. Any further increase in the current can be attributed to leakages across the contact metal-semiconductor barrier and to non-linear generation of carriers across the barrier. [18] The back interpolation of this leakage current to the zero bias (0 V) is a measure of the saturated dark current (Ids). Although the photocurrents are a few orders of magnitude larger than the thermally generated dark currents, the analysis of the photocurrent (Ips) IV function is the same as the dark current (Ids) IV plots. For dc response analysis, three sets of measurements were performed. These include (i) dark currents as a function of wall width thickness, (ii) photocurrents as a function of wall width thickness, and (iii) spectral responses as a function of wall thicknesses. These results are discussed and analyzed below.

3.5 Dark currents versus wall width thickness

To study the carrier conduction properties versus dimensionally scaling down the width of the wall structures into the nano-regime, the samples were characterized in batches. Using samples with wall widths of 200 nm, 95 nm, 75 nm, 40 nm, and 20 nm, the room temperature dark currents were measured with a probe station and digital I-V curve tracer. As the physical cross-sectional area of the wall widths was reduced from 200 nm to 20 nm, we know from Ohm's law, the resistance should increase linearly as a function of area. In other words the resistivity in units of Ω/cm² should remain constant.

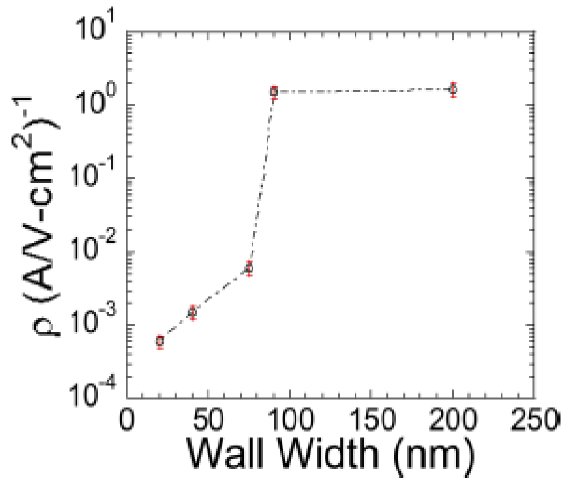

Figure 4. Plot showing resistivity characteristics as a function of down scaling the wall widths.

However, as can be seen from the Figure 4, the resistivity is not constant but drops significantly as the width of the wall is reduced below 95 nm. This suggests that there is an increase in conductivity as the wall thickness decreases from 95 nm to 20 nm. Since the number of thermally generated carriers is directly proportional to the volume of the active region, any increase in the conductivity, as wall width cross-sectional region decreases from 95 nm to 20 nm, cannot be attributed to the volume of the semiconductor material, but must be the result of a substantial increase in the carrier velocity. Confirmation of this hypothesized mechanism was obtained with the use of transient time analysis as discussed in section G. Further verification of this hypothesized mechanism was performed through transient time analysis as discussed in section 3.8.

3.6 Photocurrents versus wall width thickness

DC steady state photocurrents were measured using a 365 nm wavelength, 1.132 W/cm2 argon-ion laser and a 633 nm wavelength, 3.96 W/cm2 HeNe laser. The laser beam spot diameter was less than 8 μm and was focused within the active region of the electrode spacing covering several wall structures. By using 365 nm and 633 nm wavelengths, a more complete insight into absorption and carrier transport as a function of wall thickness can be achieved. At 365 nm,

Approved for public release: distribution is unlimited.

absorption occurs within the top first 10 nm of the Si wall structures with heights of 1500 nm. For 633 nm the total photon absorption extends through the entire wall height. Figure 5(a) and 5(b) show the conductivity versus wall thickness profiles.

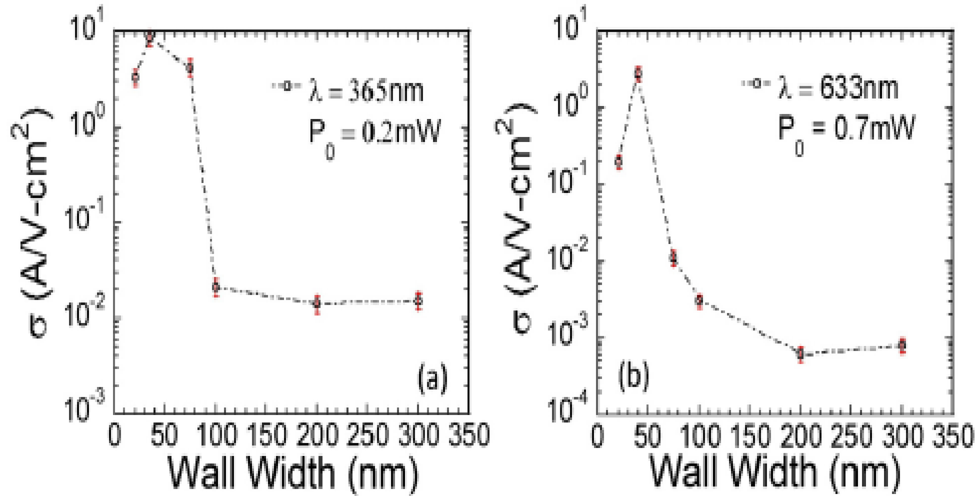

Figure 5. Plots of photoconductivity characteristics as a function of down scaling the wall widths (a) for λ=365nm; (b) for λ=633nm

As can be noted from the figures, a peak in the conductivity occurs around the 40 nm wall physical width of the samples followed by a decrease in the 25 nm wall width sample. The significance of this can be discussed through the effects of strain on the structure on the mobility of the carriers as the dimensions are reduced in section 3.8.

3.7 Transient time response measurements and analysis

The schematic of the pulsed carrier transport experiment is shown in Figure 6.

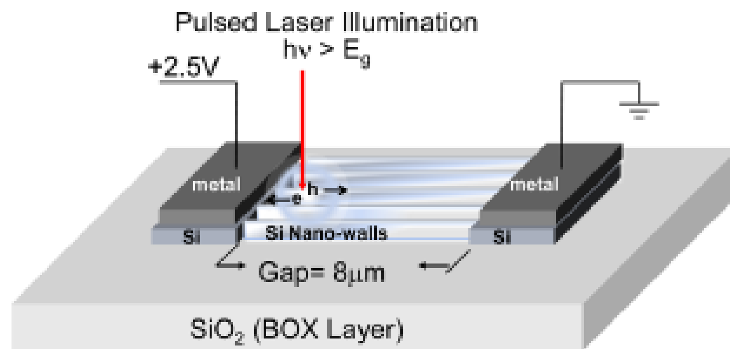

Figure 6. Schematic configuration of a wall structured MSM device used for carrier time response measurements

When a narrow pulse of light strikes the wall structured active region of the device near the left electrode as shown in Figure 6, equal number of electrons and holes are generated and are then subjected to diffusion and drift forces in a presence of an electric field. Based on the experimental configuration the electrons will be rapidly collected near the positively biased electrode and the holes will have to travel the entire active region to the negatively biased electrode. From the measured time response signal profile at the opposite electrode, the hole transient time limited carrier velocity can be determined, provided the carrier lifetime is greater than the total transit time. If the optical pulse of light strikes near the opposite electrode, the holes will be rapidly collected and the electrons would have to transit through the active region, thus the measured signal at the opposite electrode would be electron transit time limited.

The pulsed response measurements were taken using 150-fs duration excitation at $\lambda = 400$ nm from a cw mode-locked Ti:Al_2O_3 laser (doubled for the short wavelength, 0.2 mW average power at a 77 MHz repetition rate). The wall structured MSM devices were probe tested using an 18 GHz probe and a high-speed digital sampling oscilloscope with an approximately 1 ps resolution capability. The laser spot size was 1 µm in diameter and the electrode gaps were 8 µm. Normal incidence was used for the experiment. The time response measurements were taken for low electric field strengths 3×10^3V/cm, (2.5 V across 8 µm gap) thus avoiding velocity saturation.

Before the experimental data and analysis is provided it is useful to review the three primary factors that can impact the carrier transport through a semiconductor region. These factors are:

- Field dependent velocity of carriers through the active region. At high E-fields, the velocities of both electrons and holes in Si saturate at about 1×10^7 cm/s, [19] provided the field within the electrodes exceeds the saturation value for most of its length, we can assume that the carriers move with an average velocity drift. Velocity saturation is not an issue in our experiment since the applied field is much lower than what is required for saturation.

- Diffusion of carriers in the active region. The time it takes for carriers to diffuse a distance d is $\tau_{diff} = d^2/2D$ where D is the carrier diffusion coefficient. The diffusion of carriers becomes a two dimensional process as the thickness of the Si wall-structures is reduced and carriers are physically constricted in movement by the Si/SiO^2 interfaces from all sides.

- Junction and parasitic capacitance effects. A metal-semiconductor junction under reverse bias exhibits a voltage-dependent capacitance caused by the variation in stored charge at the junction represented by the relation $C_j=A/2(2e\varepsilon_s N_d)^{1/2}V^{-1/2}$, where the parameters have their usual meaning. This capacitance is usually quite small for MSM device structures as a result of their planar electrode design. There are also parasitic circuit capacitances associated with the probing and

cabling that usually dominate the electrical response as well as the limiting response of the electronics. For this study all film devices have an identical $\tau_{circuit}$ limitation.

Figure 6 represents the schematic with bias polarity of our experiment in which the left electrode polarity is positive and the right electrode is ground. With this bias configuration once a pulse of light with a spot size <1 µm, as in the case of our experiment, strikes within the active region, the holes travel towards the right electrode and the electrons travel in the opposite direction towards the left electrode.

Figure 7 shows the experimental results of the time response measurements for *~200* nm, *~95* nm, *~40* nm and *~20* nm thick wall devices for both electron and hole dominated signals. From a first pass, as can be seen from these plots, as the thickness of the film decreased, the time response signal decays faster. In particular in the case of the *~40* nm and *~20* nm thick walls the signal decays over an order of magnitude faster over the *~200* nm sample for both electrons and holes. The rise time is of the signals is important since it gives direct insight to the carrier mobility. The rise time (t_d) is defined as is the time-lapse from moment when the pulse of light strikes one end of the active region of the MSM, near one electrode, and the moment when the photo-generated carrier signal is detected at the opposite electrode. From the rise time data we can now determine the carrier mobilities as a function of thickness as follows:

From the experimental time response measurements we can calculate the average carrier velocities by applying the given relation, $v_{\text{(Carrier-Velocity)}}$ = (Electrode gap)/t_d (cm/s) where t_d is the average time it takes for the pulsed carrier signal to cross the electrode gap distance. The pulse travels in the presence of a field and expands from its originating point due to diffusion. In this case we are ignoring the RC time delay that the pulsed signal experiences once it reaches the edge of the depletion region near the electrodes since the widths of the depletion regions are very small in the submicron range compared to the electrode gap which is ~8µm in length.

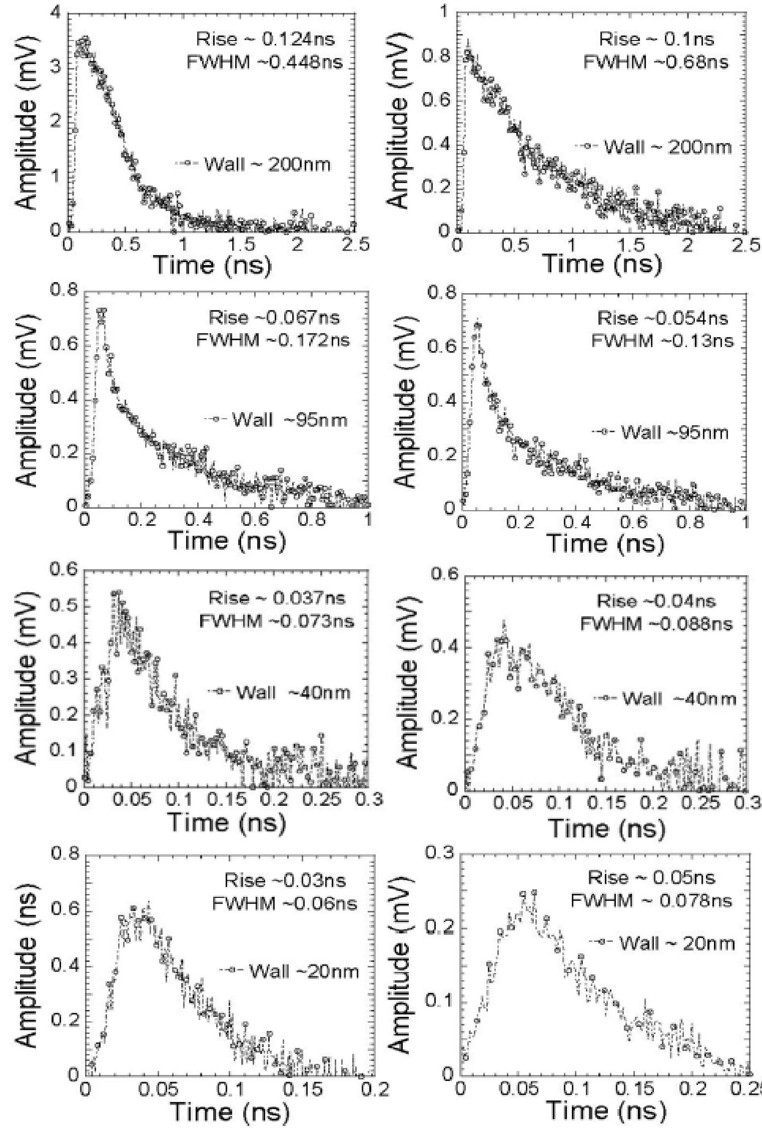

Figure 7. Measured time response signals of 200nm wall (row-1), 95nm wall (row-2), 40nm wall (row-3) and 20nm wall (row-4)

By definition the average carrier mobility can be written as,

$$\mu_{avg} = v_{(\text{Avg Carrier-Velocity})}/[V_{bias}/(\text{Electrode})]$$

where V_{bias} is the external bias applied to the electrodes.

Figure 8 shows a plot of average field dependent electron and hole limited mobility values using experimental values of rise time, t_d, and the above expression as a function of film thickness.

Approved for public release: distribution is unlimited.

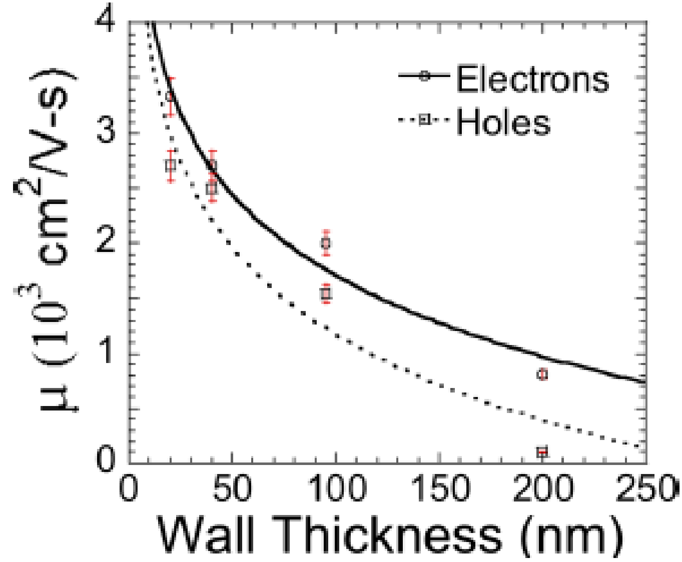

Figure 8. Carrier mobility values calculated from direct measure of rise time values as a function of wall thickness.

We know that the carrier transport of electrons and holes in the thickest wall sample (*~200* nm) is essentially similar to the transport properties in bulk silicon. However we observe a considerable increase in low filed dependent mobility values below ~*75* nm wall thicknesses. Recall the fact that we actually have a much narrower effective cross-sectional regions form which carriers propagate due to the repulsive nature of the boundary at the Si/SiO_2 interface, and the carrier profile tends to peak a certain distance away from the interface close to the center of the wall structures. Therefore we believe that quantum confinement effects play a key role in the carrier mobilities of both electrons and holes. A detailed theoretical model is described in the next section which tends to explain our experimental results.

3.8 Theoretical Modeling using strain effects to explain rise in electron and hole mobility

If we consider a total valence-band hole concentration n_v then, the light-hole (n_{LH}) and the heavy-hole (n_{HH}) concentration will satisfy the charge-conservation relation $n_{LH} + n_{HH} = n_v$, where

$$n_\sigma = \frac{g_\Gamma g_s}{V} \sum_{\boldsymbol{k}} \left[1 + exp\left(\frac{E_k^\sigma \mp \eta \Delta E_{str}^v - u_v}{k_B T}\right)\right]^{-1} \approx 2g_\Gamma \left(\frac{m_\sigma^* k_B T}{2\pi\hbar^2}\right)^{3/2} exp\left(\frac{u_v \pm \eta \Delta E_{str}^v}{k_B T}\right),$$

where the subscript σ takes HH or LH and the upper (lower) sign corresponds to HH (LH) state. In the above expressions, the approximations are made for high temperatures, V is the volume of the silicon film, T is the system temperature, the zero energy is chosen at the middle point between the split pair of light-hole and heavy-hole bands, **k** is the three dimensional wave vector of carriers, $g_\Gamma = 2$ (not *6* due to strain effect) is the Γ-valley degeneracy for holes and $g_s = 2$ is the spin degeneracy for both light-holes and heavy-holes. In addition, u_v, which depends on both T and n_V, is the chemical potential to be determined for valence bands, $E_k^{HH} = \hbar^2 k^2/2m_{HH}^*$ is the kinetic energy of heavy holes and $E_k^{LH} = \frac{\hbar^2 k^2}{2m_{LH}^*}$ is the kinetic energy of light holes, where $m_{HH}^* = 0.49m_0$ and $m_{LH}^* = 0.16m_0$ ($m_0$is the free-electron mass) are the effective masses for heavy holes and light holes, respectively. Additionally, ΔE_{str}^v introduced in the above expressions stands for the half of the valence-band splitting due to the existence of strain.

From the above two equations and $n_{LH} + n_{HH} = n_v$, we obtain $n_{LH}/n_v = [1 + \gamma^{3/2}\, exp(2\eta \Delta E_{str}^v/k_B T)]^{-1}$ and $n_{HH}/n_v = 1 - n_{LH}/n_v$, where $\gamma \equiv (m_{HH}^*/m_{LH}^*) > 1$. For biaxial and shear strains, [1,2] we have the valence-band splitting, given by $\Delta E_{str}^v = \pm\left\{(b^2/2)\left[\left(\epsilon_{xx} - \epsilon_{yy}\right)^2 + \left(\epsilon_{yy} - \epsilon_{zz}\right)^2 + (\epsilon_{zz} - \epsilon_{xx})^2\right] + d^2\left[\epsilon_{xy}^2 + \epsilon_{yz}^2 + \epsilon_{xz}^1\right]\right\}^{1/2}$, where the upper sign is for the compressive strain while the lower sign for the tensile strain in the direction perpendicular to the interface of silicon and silicon-dioxide materials, *b* and *d* are the optical deformation potentials, and $\epsilon_{jj'}$ represents the strain tensor in the three dimensional space with *j*, *j'* = *x*, *y*, and *z*, the diagonal matrix elements ϵ_{jj} are associated with biaxial strain, and the off-diagonal matrix elements $\epsilon_{jj'}$with *j ≠ j'* correspond to contributions from the shear strain. For silicon crystals, we have *b= -2.33* eV and *d= -4.75* eV.

The values of η can be scaled as $\eta = (1/L)\{\min(L, 2D_s)\}$, where L is the film thickness and D_s is the strain buffing depth due to lattice mismatch between embedded Si crystal and surrounding amorphous SiO_2 material at their interface, and $L - 2D_s > 0$ represents the film effective thickness free of localized trapping centers [19].

If we choose the *z* direction as the direction perpendicular to the interface for biaxial strain we simply get $\epsilon_{xx} = \epsilon_{yy} = \epsilon_\parallel$, $\epsilon_{zz} = \epsilon_\perp$, and $\epsilon_{ij} = 0$ for $i \neq j$, [19] where$\epsilon_\parallel = \left(a_{\parallel,Si}/a_{Si} - 1\right)$, $\epsilon_\perp = \left(a_{\perp,Si}/a_{Si} - 1\right)$. Moreover, the perpendicular lattice constant $a_{\perp,Si}$ is related to the parallel lattice constant $a_{\parallel,Si} = \bar{a}_{SiO_2}$ by $a_{\perp,Si} = a_{Si}\left[1 - (2c_{12}/c_{11})\left(\bar{a}_{SiO_2}/a_{Si} - 1\right)\right]$, where $c_{11} = 16.75 \times 10^{10}$ N/m^2, and $c_{12} = 6.5 \times 10^{10}$ N/m^2 are the elastic constants of silicon. For silicon and silicon-dioxide, we have $\bar{a}_{SiO_2} = (2 \times 4.914 + 5.405)/3 = 5.078$ Å and $a_{Si} = 5.431$ Å for amorphous silicon-dioxide materials. Therefore, we obtain $a_{\perp,Si}/a_{Si} = 1.050$. This leads to $\epsilon_\parallel = -0.065$ (compressive), $\epsilon_\perp = 0.05$ (tensile), and $2\epsilon_\parallel + \epsilon_\perp = -0.08$.

The total mobility $\mu_{\rm v}$ for holes can be expressed as

$$\mu_{\rm v} = \left(\frac{n_{\rm LH}}{n_{\rm v}}\right)\frac{e\tau_{\rm LH}}{m_0}\left[\frac{m_0}{m^*_{\rm LH}} + \Delta\left(\frac{m_0}{m^*_{\rm LH}}\right)\right] + \left(\frac{n_{\rm HH}}{n_{\rm v}}\right)\frac{e\tau_{\rm HH}}{m_0}\left[\frac{m_0}{m^*_{\rm HH}} + \Delta\left(\frac{m_0}{m^*_{\rm HH}}\right)\right] \approx \left(\frac{n_{\rm LH}}{n_{\rm v}}\right)\frac{e\tau_{\rm LH}}{m^*_{\rm LH}} + \left(\frac{n_{\rm HH}}{n_{\rm v}}\right)\frac{e\tau_{\rm HH}}{m^*_{\rm HH}}$$

$$\approx \left(\frac{e\tau_{\rm LH}}{m^*_{\rm LH}} + \gamma^{3/2}\frac{e\tau_{\rm HH}}{m^*_{\rm HH}}\right)\frac{1}{(1+\gamma^{3/2})} - \gamma^{3/2}\left(\frac{e\tau_{\rm LH}}{m^*_{\rm LH}} - \frac{e\tau_{\rm HH}}{m^*_{\rm HH}}\right)\left[\frac{\exp(2\eta\Delta E^v_{str}/k_BT)-1}{(1+\gamma^{3/2})^2}\right]$$

$$\approx \mu_v^{(0)}\left[1 - \frac{\eta(2\Delta E^v_{str}/k_BT)\gamma^{\frac{1}{2}}(\gamma-1)}{(1+\gamma^{1/2})(1+\gamma^{3/2})}\right] + \mathcal{O}\left[\left(\frac{\Delta E^v_{str}}{k_BT}\right)^2\right],$$

i.e., $\left(\mu_v/\mu_v^{(0)} - 1\right) \propto \eta \propto 1/L$, where $\mu_v^{(0)} = (e\bar{\tau}_{\rm v}/m^*_{\rm LH})(1+\gamma^{1/2})(1+\gamma^{3/2})$ is the valence band mobility for $\eta \to 0$, $1/\bar{\tau}_{\rm v} = (1/2)(1/\tau_{\rm LH} + 1/\tau_{\rm HH})$ (with $\tau_{\rm LH} \approx \tau_{\rm HH} \approx \bar{\tau}_{\rm v}$), $|\Delta E^v_{str}| \ll k_BT$ is assumed, the changes in the hole effective masses by strain have been neglected, $\tau_{\rm LH}$ and $\tau_{\rm HH}$ are the scattering times for light and heavy holes, respectively. It is clear that μ_v increases with $1/L$ for the tensile strain ($\Delta E^v_{str} < 0$) in the direction perpendicular to the interface of silicon and silicon-dioxide materials, as observed by us in Figure 9.

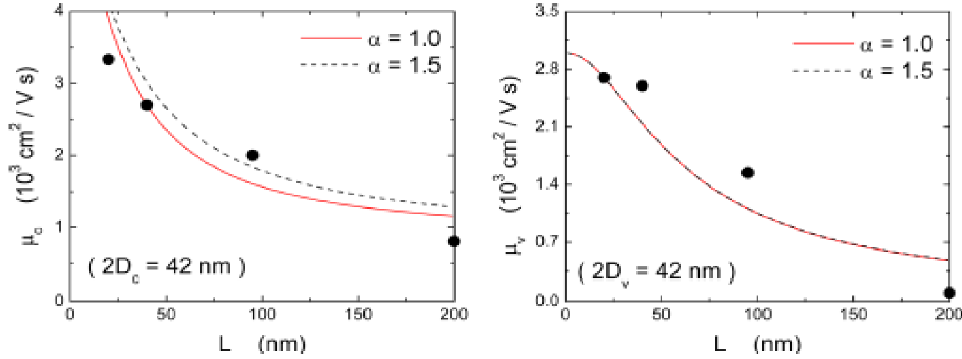

Figure 9. Theoretical modeling for electron (left panel) and hole (right panel) mobilities ias functions of wall thinckness L with α= 1.0 (red solid curves) and 1.5 (black dashed curves) and their comparisons with experimental data (black dots in both panels

d electron concentration n_c, the electron chemical potential u_c, which depends on both T and n_c, is decided from

$$n_c = \sum_{\xi=X,L} n_\xi = \frac{g_s}{V}\sum_{\xi=X,L} g_\xi \sum_k \left[1 + exp\left(\frac{E^\xi_k + E^\xi_G - u_c}{k_BT}\right)\right]^{-1}$$

$$\approx 2\sum_{\xi=X,L} g_\xi \left(\frac{m^*_\xi k_BT}{2\pi\hbar^2}\right)^{3/2} exp\left(\frac{u_c - E^\xi_G}{k_BT}\right) \quad ,$$

where the high-temperature approximation is made in the above expression, $E_G^\xi = \varepsilon_G^\xi(T) + \eta' \Delta E_G^\xi$ is the bandgap energy of strained silicon crystals, which depends on T and the hydrostatic part of the strain, ε_G^ξ stands for the bandgap energy of unstrained silicon crystals, $g_{X,L} = 2$ (not *6* due to strain effect) represents the X (in <100> direction) and L (in <111> direction) valley degeneracy for electroncs at the two minima of conduction band, $E_G^\xi = \hbar^2 k^2/2m_\xi^*$ is the kinetic energy of electrons and m_ξ^* is the transverse effective mass of conduction-band electrons with $m_X^* = 0.19m_0$ and $m_L^* = 0.1m_0$. The T dependence of $\varepsilon_G^\xi(T)$ (based on the Bose-Einstein phonon model) is given by $\varepsilon_G^\xi(T) = \varepsilon_G^\xi(0) - 2\alpha_B\Theta_B[coth(\Theta_B/2T) - 1]$, where $\alpha_B = 2.82 \times 10^{-4}$ eV/K is a coupling constant, $k_B\Theta_B$ is a typical phonon energy with $\Theta_B = 351$ K, $\varepsilon_G^X(T) = 1.12$ eV and $\varepsilon_G^L(T) = 2.4$ eV at $T = 300$ K for the *X* and *L* valleys. Moreover, the strain part [2] of the bandgap energy ΔE_G^ξ is calculated as $\Delta E_G^\xi = \Xi_d^{(\xi)} Tr(\overleftrightarrow{\epsilon}) + \Xi_u^{(\xi)} \vec{e}_\xi \cdot \overleftrightarrow{\epsilon} \cdot \vec{e}_\xi + aTr(\overleftrightarrow{\epsilon})$, where $\Xi_d^{(X,L)}$ and $\Xi_u^{(X,L)}$ are the deformation potentials of the conduction band for an indirect-gap silicon crystal ($\Xi_d^{(X)} = 1.1$ eV, $\Xi_u^{(X)} = 10.5$ eV for the X valley and $\Xi_d^{(L)} = -7.0$ eV, $\Xi_u^{(L)} = 18.0$ eV for the L valley), $a = 2.1$ eV is the difference of the deformation potentials of conduction and valence bands at two different valleys due to hydrostatic component of the strain for the silicon crystal, and $\vec{e}_\xi$ is the unit vector pointing to the specific X or L valley. It is clear from the above equation that $\Delta E_G^\xi < 0$ for the tensile strain and $\xi = X$ or L .

The change in the bandgap energy by strain also affects the effective mass of conduction band, given by [20] also see [21-33].

$$\Delta\left(\frac{m_0}{m_\xi^*}\right) \approx -\frac{E_P(2\epsilon_\parallel+\epsilon_\perp)\eta'}{\varepsilon_G^\xi(T)+\Delta_0/3}\left[2 + \frac{3a+3\Xi_d^{(\xi)}+\Xi_u^{(\xi)}}{\varepsilon_G^\xi(T)+\Delta_0/3}\right] + \mathcal{O}[(2\epsilon_\parallel + \epsilon_\perp)^2] \,,$$

where we have neglected the shear strain and assumed a weak strain with $|2\epsilon_\parallel + \epsilon_\perp| \ll 1$, $\Delta_0 =$ 44 meV is the spin-orbit splitting and $E_P = 21.6$ eV is the Kane energy parameter.

The total mobility μ_c of conduction-band electrons is obtained as

$$\mu_c = \left(\frac{n_X}{n_c}\right)\frac{e\tau_X}{m_0}\left[\frac{m_0}{m_X^*} + \Delta\left(\frac{m_0}{m_X^*}\right)\right] + \left(\frac{n_L}{n_c}\right)\frac{e\tau_L}{m_0}\left[\frac{m_0}{m_L^*} + \Delta\left(\frac{m_0}{m_L^*}\right)\right] \approx \frac{e\tau_X^0}{m_0}\left[\frac{m_0}{m_X^*} + \Delta\left(\frac{m_0}{m_X^*}\right)\right]^{1+\alpha}$$

$$= \frac{e\tau_X^0}{m_X^*}\left\{1 + (1+\alpha)\left(\frac{m_X^*}{m_0}\right)\Delta\left(\frac{m_0}{m_X^*}\right) + \frac{\alpha}{2}(1+\alpha)\left(\frac{m_X^*}{m_0}\right)^2\left[\Delta\left(\frac{m_0}{m_X^*}\right)\right]^2 + \cdots\right\}$$

$$= \frac{e\tau_X}{m_X^*} - \eta'(1+\alpha)\left(\frac{e\tau_X}{m_0}\right)\frac{E_P(2\epsilon_\parallel+\epsilon_\perp)}{\varepsilon_G^X(T)+\Delta_0/3}\left[2 + \frac{3a+3\Xi_d^{(X)}+\Xi_u^{(X)}}{\varepsilon_G^X(T)+\Delta_0/3}\right] + \mathcal{O}[(2\epsilon_\parallel + \epsilon_\perp)^2]$$

$$= \mu_c^{(0)}\left\{1 - \eta'(1+\alpha)\left(\frac{m_X^*}{m_0}\right)\frac{E_P(2\epsilon_\parallel+\epsilon_\perp)}{\varepsilon_G^X(T)+\Delta_0/3}\left[2 + \frac{3a+3\Xi_d^{(X)}+\Xi_u^{(X)}}{\varepsilon_G^X(T)+\Delta_0/3}\right]\right\} + \mathcal{O}[(2\epsilon_\parallel + \epsilon_\perp)^2] \,,$$

i.e., $(\mu_c/\mu_c^0 - 1) \propto \eta' + \mathcal{O}(\eta'^2) \propto 1/L + \mathcal{O}(1/L^2)$ (using $\eta' \sim \eta$), where we assume $\tau_\xi = \tau_\xi^0(m_0 m_\xi^*)^\alpha$ with α labelling the mass dependence in the scattering rate, $\mu_c^{(0)} \approx e\tau_{\mathrm{X}}/m_{\mathrm{X}}^*$ is the conduction-band mobility for $\eta' \to 0, \tau_{X,L}$ represents the scattering times of conduction-band electrons at two different valleys and the high-energy L valley has been assumed depopulated. It is clear that the electron mobility increases with $1/L^2$ in our system with $(2\epsilon_\parallel + \epsilon_\perp) = -0.08$, as observed by us in Figure 9.

4 RESULTS AND DISCUSSION

Table 1 and 2 below show the results of the theoretical calculations. As was previously shown in Figure 9, the comparisons between experiment and theory are within 10% which is a very good.

Table 1. Model parameters used in calculating mobility of electrons in strained Si WALL Structures.

μ_c^{max} $(cm^2/V\cdot s)$	$\mu_c^{(0)}$ $(cm^2/V\cdot s)$	λ_c (nm)	$2D_c$ (nm)
5500	806	15	42

Table 2. Model parameters used in calculating mobility of holes in strained Si wall structures.

μ_v^{max} $(cm^2/V\cdot s)$	$\mu_v^{(0)}$ $(cm^2/V\cdot s)$	λ_v (nm)	$2D_v$ (nm)
3000	100	143	42

As can be noticed from both the experiment and theory, the carrier concentration includes both the doping and photo-excitation contributions. If the sample is undoped, we can simply neglect the impurity scattering and have $n_c = n_v$. The optical-phonon scattering and the inter-valley scattering are only important at high temperatures, while the acoustic-phonon scattering becomes more significant at low temperatures. The surface-roughness scattering, on the other hand, is largely independent of temperature. In the narrowest wall devices, a considerable increase in conductivity was observed as a result of higher carrier mobilities due to lateral constriction. The strain effects, which include the reversal splitting of light- and heavy- hole bands as well as the decrease of conduction-band effective mass by reduced Si bandgap energy, are formulated in our microscopic model for explaining the experimentally observed enhancements in both conduction- and valence-band mobilities with reduced Si wall thickness. Specifically, the enhancements of the valence-band and conduction-band mobilities are found to be associated with different aspects of physical mechanisms. The role of the biaxial strain buffering depth is elucidated and its importance to the scaling relations of wall-thickness is reproduced theoretically, i.e., $1/L^2$ for electrons and $1/L$ for holes.

5 CONCLUSION

The semiconductor processing, fabrication and the resulting carrier transport characteristics of MSM devices fabricated as wall like structures in silicon on insulator technology were reported. MSM device dark current, DC photocurrents, and the time response of car-rier transport were investigated. The resulting conducting channels were actually smaller than their physical dimensions, a result of depletion of carrier near the interfaces. As the physical channel widths were reduced by oxidation, strain was produced near the interface and strained lattice became a significant portion of the conducting channel. The increase in mobilities for both holes and electrons stemming from the strained silicon resulted in a dramatic increase in carrier mobility for both electrons and holes as the physical channel width was reduced from 200 nm to 20 nm. The theoretical model incorporating the effects of strain present in these nanoscale MSM devices compared favorably with experimental results, showing that hole mobilities increased with decreasing L. Additionally, if these elec-tron and hole mobilities can be retained with the application of gate electrodes, then this technique may yield a much simpler path towards high performance CMOS, both n-channel and p-channel, than current techniques for either planer ultra-thin body FETs or FinFETs.

REFERENCES

[1] A. Holmes-Siedle and L. Adams, **Handbook of Radiation Effects**, 2nd edition, Oxford University Press, Oxford UK, 2002.

[2] B. Vandana and M. S. Kumar, "Study of VLSI Bulk CMOS and SOI Technologies," *International Journal Scientific & Research Publications* **3**, 2, pp. 2250-3153, 2013.

[3] S. M. Ramey and D. K. Ferry, "Threshold voltage calcuation in ultra-thin film SOI MOSFETs using the effective potential," *IEEE Transactions on Nanotechnology* **2**, pp. 121-125, 2003.

[4] S. Bhattacharya and K. P. Ghatak, **Effective Electron Mass in Low-Dimensional Semiconductors**, Springer, New York, 978-3-642-31247-2/0933-033X, 2013.

[5] S. Schmitt-Rink, D. S. Chemla and D. A. B. Miller, "Linear and nonlinear optical propoerties of semiconductor quantum wells," *Advances in Physics* **38**, Issue 2, p. 89-91, 1989.

[6] S. Kundu and A. Sreekhar, **Nanoscale CMOS VLSI Circuits: Design for Manufacturability**, McGraw-Hill Professional, 978-0071635196/007163519X, 2010.

[7] S. W. Bedell, A. Khakifirooz and D. K. Sadana, "Strain scaling for CMOS," *MRS Bulletin* **39**, 2, p. 131-137, 2014.

[8] A. K. Sharma, R. Prinja and S. R. J. Brueck, "Effects of dimensional scaling on the electronic transport properties of silicon nanofilms and nanowires," *5th IEEE Conference Nanotechnology* **2**, pp. 746-749, Nagoya, Japan, 2005.

[9] W. Windl, M. M. Bunea, R. Stumpf, S. T. Dunham and M. P. Masquelier, "First-Principles Study of Boron Diffusion in Silicon," *Physical Review Letters* **83**, Issue 21, pp. 4345-4349, 1999.

[10] W. Hansch, T. Vogelsang, R. Kircher and M. Orlowski, "Carrier transport near the Si/SiO2 interface of a MOSFET," *Solid-State Electron*. **32**, Issue 10, pp. 839-841, 1989.

[11] E. S. Yang, **Microelectronic Devices**, McGraw-Hill, Inc., 0-07-072238-2, 1988.

[12] D. M. Fleetwood, S. T. Pantelides and R. D. Schrimpf, **Defects in Microelectronic Materials and Devices**, CRC Press, pp. 736-759, 2008.

[13] S. R. J. Brueck, "Optical and Interferometric Lithography - Nanotechnology Enablers," *Proceedings of the IEEE*, Vol. **93**, 10, pp. 1704-1721, 2005.

[14] S. H. Zaidi and S. R. J. Brueck, "Interferometric lithography for nanoscale fabrication," *Proceedings SPIE* **3618**, 2, p. 2019-2021, 1999, San Jose, CA.

Approved for public release: distribution is unlimited.

[15] S. H. Zaidi, S. R. J. Brueck, F. M. Schellenberg, R. S. Mackay, K. Uekert and J. J. Persoff, “Interferometric lithography exposure tool for 180-nm structures,” *Proceedings SPIE* **3048**, pp. 248-252, Santa Clara, CA, 1997.

[16] S. Alexandrova, A. Szekeres and E. Halova, “Defects in SiO2/Si Structures Formed by Dry Thermal Oxidation of RF Hydrogen Plasma Cleaned Si,” *Materials Science and Engineering* **15**, 012037, 2010.

[17] G. Duscher, S. J. Pennycook, N. D. Browning, R. Rupangudi, T. Takoudis, H-J Gao and R. Singh, “Structure, composition and strain profiling of Si/SiO2 interfaces,” *AIP Conference Proceedings* **449**, p. 191, 1998.

[18] S. Vitkavage, E. A. Irene and H. Z. Massoud, “An investigation of SiSiO2 interface charges in thermally oxidized (100), (110), (111), and (511) silicon,” J*ournal of Applied Physics*, vol. **68**. http://doi.org/10.1063/1.347042, 1990.

[19] J. Becker, E. Fretwurst and R. Klanner, “Measurements of charge carrier mobilities and drift velocity saturation in bulk silicon of <111> and <100> crystal orientation at high electric fields,” *Solid State Electron*, **56**, p. 104-110, 2011.

[20] J. R. Haynes and W. Shockley, “The Mobility and Life of Injected Holes and Electrons in Germanium,” *Physics Review* **81**, p. 835, 1951.

[21] G. K. Cellar, S. Cristoloveanu, J. G. Fossum, F. Gamiz and K. Izumi, “Silicon-on-Insulator Technology and Devices XII,” 2005: *Proceedings of the International Symposium, Electro-chemical Society*, 1566774616/978-1566774511, Quebec, Canada, 2005.

[22] M. Grundmann, **The Physics of Semiconductors**, 2nd edition, Springer-Verlag, Berlin Heidelberg, 2010.

[23] B. Bahder, “Electron band structure of rare-earth metal: Tb(0001),” *Physics Review* B 41, 11922, 1990.

[24] F. Schäffler, “High-mobility Si and Ge structurese,” *Semiconductor Science Technology* **12**, 1515, 1997.

[25] Y. Sun, S. E. Thompson and T. Nishida, “Physics of strain effects in semiconductors and metal-oxide-semiconductor field-effect transistors,” *Journal of Applied Physics* **101**, 104503, 2007.

[26] E. G. Barbagiovanni, D. J. Lockwood, P. J. Simpson, L. V. Goncharova, “Quantum confinement in Si and Ge nanostructures: Theory and experiment,” *Applied Physics Review* **1**, 011302, 2014.

[27] H. Ohta, T. Watanabe, and I. Ohdomari, "Strain distribution around SiO2/Si interface in Si nanowires: A Molecular Dynamics Study," *Japanese Journal of Applied Physics* **46**, p. 3277, 2007.

[28] D. E. Aspnes and M. Cardona, "Strain dependence of effective masses in tetrahedral semiconductors," *Physics Review* B, **17**, Issue 2, p. 726, 1978.

[29] M. V. Fischetti and S. E. Laux, "Band structure, deformation potentials, and carrier mobility in strained Si, Ge, and SiGe alloys," *Journal of Applied Physics* **80**, p. 2234, 1996.

[30] D. H. Huang, P. M. Alsing, T. Apostolova and D. A. Cardimona, "Coupled energy-drift and force-balance equations for high-field hot-carrier transport," *Physics Review* B **71**, 195205, 2005.

[31] G. Gumbs and D. H. Huang, **Properties of Interacting Low-Dimensional Systems**, Wiley-VCH, 1st edition, Verlag GmbH & Co. KGaA, Weinheim, Germany, 2011.

[32] T. Ando, A. B. Fowler and F. Stern, "Electronic properties of two-dimensional systems," *Review Modern Physics* **54**, p. 437, 1982.

[33] D. H. Huang and D. A. Cardimona, "Effects of off-diagonal radiative-decay coupling on electron transitions in resonant double quantum wells," *Physics Review* A **64**, 013822, 2001.

LIST OF ACRONYMS

BOE	Buffered oxide etch
CMOS	Complementary Metal Oxide Semiconductor
DC	Direct current
FET	Field Effect Transistor
FinFET	Fin shaped Field Effect Transistor
FM	Fresnal Mirror
HH	Heavy hole
Ids	Dark current
IL	Interferometric Lithorgraphy
Ips	Photocurrent
ITRS	International Technology Roadmap for Semiconductors
LH	Light hole
MSM	Mobile Service Manager
MSM	Metal Si/nanowall Metal
nFET	n-type FET
pFET	p-type FET
Q_f	Fixed Charge
Q_{it}	Interface Trapped Charge
Q_{oT}	Oxide Trapped Charge
RIE	Reactive ion-etching
SEM	Scanning Electron Microscope

SGOI	SiGe on-insulator
SOI	Silicon-on-Insulator
sSOI	Strained Silicon-on-Insulator
VDD	Voltage Drain Supply
VLSI	Very Large Scal Integration

Approved for public release: distribution is unlimited.

DISTRIBUTION LIST

DTIC/OCP 8725 John J. Kingman Rd, Suite 0944 Ft Belvoir, VA 22060-6218	1 cy
AFRL/RVIL Kirtland AFB, NM 87117-5776	2 cys
Official Record Copy AFRL/RVSW/Ashwani Sharma	1 cy